



Modeling the BOLD correlates of competitive neural dynamics



James Bonaiuto^{a,b,c,*}, Michael A. Arbib^{b,c,d}

^a Division of Biology, California Institute of Technology, Pasadena, CA 91225, USA

^b Neuroscience Program, University of Southern California, Los Angeles, CA 90089-2520, USA

^c USC Brain Project, University of Southern California, Los Angeles, CA 90089-2520, USA

^d Computer Science Department, University of Southern California, Los Angeles, CA 90089-2520, USA

ARTICLE INFO

Article history:

Received 13 June 2013

Received in revised form 2 September 2013

Accepted 4 September 2013

Keywords:

Neural network model
fMRI, decision-making
Winner-take-all
Synthetic brain imaging

ABSTRACT

Winner-take-all models are commonly used to model decision-making tasks where one outcome must be selected from several competing options. Related random walk and diffusion models have been used to explain such processes and apply them to psychometric and neurophysiological data. Recent model-based fMRI studies have sought to find the neural correlates of decision-making processes. However, due to the fact that hemodynamic responses likely reflect synaptic rather than spiking activity, the expected BOLD signature of winner-take-all circuits is not clear. A powerful way to integrate data from neurophysiology and brain imaging is by developing biologically plausible neural network models constrained and testable by neural and behavioral data, and then using *Synthetic Brain Imaging* – transforming the output of simulations with the model to make predictions testable against neuroimaging data. We developed a biologically realistic spiking winner-take-all model comprised of coupled excitatory and inhibitory neural populations. We varied the difficulty of a decision-making task by adjusting the contrast, or relative strength of inputs representing two response options. Synthetic brain imaging was used to estimate the BOLD response of the model and analyze its peak as a function of input contrast. We performed a parameter space analysis to determine values for which the model performs the task accurately, and given accurate performance, the distribution of the input contrast–BOLD response relationship. This underscores the need for models grounded in neurophysiological data for brain imaging analyses which attempt to localize the neural correlates of cognitive processes based on predicted BOLD responses.

© 2013 Elsevier Ltd. All rights reserved.

1. Introduction

A continuing challenge for systems and cognitive neuroscience is to integrate data from animal neurophysiology and human brain imaging. While neurophysiological studies provide detailed information on the properties of a sample of neurons in a single region, brain imaging data reflects global brain activity resulting from neural population activation. Although these two sources of information are often used in developing *conceptual* models of cognitive processes, more refined analysis requires an explicit account of the coupling between these levels of data. One method that has begun to shed light on this coupling is synthetic brain imaging. This technique uses computational models of the brain regions in question based on neurophysiological data to generate simulated neuroimaging signals such as regional cerebral blood flow (rCBF) and blood oxygen level-dependent (BOLD) responses.

These can then be compared with experimental neuroimaging data in order to reinterpret imaging data in computational terms and to validate and update models of macaque circuitry.

Winner-take-all (WTA) or race models are frequently used to account for psychophysical data in decision-making tasks. Given multiple inputs, these models converge on an output corresponding to the strongest input. This makes them well suited for decision-making tasks where evidence for multiple alternatives is integrated and one must be selected. Many types of WTA models have been proposed. Neural field models implement WTA dynamics through the use of recurrent excitation and surround inhibition (Amari, 1977). Leaky accumulator models assume that evidence for different response options is integrated over time with some decay factor and a decision is made once one accumulator reaches a threshold (Usher & McClelland, 2001). Similar models have been used to interpret data from perceptual decision making tasks such as the random dot motion direction discrimination (RDMDD) task (Palmer, Huk, & Shadlen, 2005). In this task the subject observes a field of moving dots and must decide in which direction (right or left) the majority of dots are moving, and then make a saccade to the right or left target stimulus to indicate their choice. In different conditions the percentage of dots moving in the same direction, or

* Corresponding author at: Division of Biology, California Institute of Technology, Pasadena, CA 91225, USA. Tel.: +1 6263955851.

E-mail address: bonaiuto@caltech.edu (J. Bonaiuto).

coherence, is varied from 0% to 100%. Response time and accuracy vary predictably as a function of coherence (Palmer et al., 2005), allowing it to serve as an indication of task difficulty. In this paper, we perform synthetic brain imaging on a neural WTA network in order to determine the likelihood that such a model would exhibit a particular relationship between coherence and peak BOLD response.

The generic structure of a synthetic brain imaging model involves coupled neural and synaptic models that are grouped into virtual voxels or larger aggregates. The output of each synapse is summed and input to a model of neurovascular coupling, which then feeds into a vascular model to generate simulated rCBF or BOLD responses. The choice of neural and synaptic model depends on the data that the overall model is intended to address. Early synthetic brain imaging approaches used simple firing rate neural models (Arbib, Bischoff, Fagg, & Grafton, 1995) while later models used mean field approximations (Corchs & Deco, 2002, 2004), leaky integrate-and-fire models (Deco, Rolls, & Horwitz, 2004), and compartmental models (Riera, Wan, Jimenez, & Kawashima, 2006). A suggestion of the earliest synthetic brain imaging study (Arbib et al., 1995) which was used by later approaches (Riera et al., 2006; Tagamets & Horwitz, 1998) was that the hemodynamic response reflected synaptic activity rather than the spiking output of a region. This is in agreement with recent studies in monkeys and rats that suggest that the BOLD response reflects synaptic activity in both pyramidal cells and interneurons (Cauli et al., 2004; Goense & Logothetis, 2008; Pelled et al., 2009). Our model of synthetic brain imaging therefore uses integrated synaptic activity in pyramidal cells and interneurons to generate the blood flow inducing signal. We also tested the effect of using only integrated excitatory synaptic activity, but the results were not significantly different and we therefore do not report on these simulations here.

1.1. Neural and synaptic models

Synaptic models in previous approaches have ranged from the absolute values of connection weights multiplied by presynaptic firing rate (Arbib et al., 1995; Tagamets & Horwitz, 1998) to simple models of synaptic conductances for basic receptor types (AMPA, NMDA, GABA_A, GABA_B) (Deco et al., 2004). Given the assumption that activity-driven increase in blood flow is triggered by synaptic activity, models that generate simulated BOLD responses should incorporate synapses with, to the extent that data permits, realistic conductance amplitudes and time courses. The recent rise of fMRI on awake, behaving monkeys (Kagan, Wilke, & Andersen, 2009; Nelissen, Luppino, Vanduffel, Rizzolatti, & Orban, 2005) provides a unique opportunity to calibrate models using synthetic brain imaging since both neurophysiological and hemodynamic data are available. Several studies have performed fMRI on monkeys while administering neuropharmacological drugs such as muscimol, a GABA agonist (Wilke, Kagan, & Andersen, 2009, 2010). These conditions can be directly simulated by synaptic models that allow the conductance of a particular synapse type to be altered.

In this paper we will apply synthetic brain imaging to networks which employ conductance-based synapse models for AMPA, NMDA, GABA_A, and GABA_B synapse types. We sum the synaptic currents of each type (AMPA, NMDA, GABA_A, and GABA_B) and input the total synaptic current into the adaptive exponential leaky integrate-and-fire (LIF) neural model (Brette & Gerstner, 2005). Neurons are grouped into excitatory and inhibitory populations with projections within and between populations.

1.2. Neurovascular coupling

Early approaches to modeling the neurovascular coupling mechanism focused on the metabolic basis for the BOLD signal (Jueptner & Weiller, 1995). Based on the reasoning that increased

synaptic activity resulted in increased neural metabolism with a consequent increase in local blood flow, these models integrated the total synaptic activity in a modeled region in order to compute a qualitative measure of rCBF (Arbib et al., 1995; Tagamets & Horwitz, 1998). In order to compute synaptic activity in a voxel or volume, $p(t)$, these models summed the product of each neuron's input with the absolute value of its connection weight (to include the effects of inhibitory synapses on rCBF). Similarly, later models used the sum of the absolute value of synaptic currents (Deco et al., 2004). However this may not be an appropriate measure of synaptic activity since each synaptic current goes to zero as the membrane potential approaches its associated reversal potential. Therefore, Izhikevich and Edelman (2008) use the sum of synaptic conductances:

$$p(t) = \sum_m (g_{\text{AMPA}}^m(t) + g_{\text{NMDA}}^m(t) + g_{\text{GABA}_A}^m(t) + g_{\text{GABA}_B}^m(t)) \quad (1)$$

where $g_n^m(t)$ is the synaptic conductance of receptor type n in neuron m at time t . More detailed studies have modeled neural metabolism, including glucose and oxygen (Sotero, Trujillo-Barreto, Jimenez, Carbonell, & Rodriguez-Rojas, 2009) and ATP consumption (Aubert, Pellerin, Magistretti, & Costalat, 2007), however these studies did not involve networks of neurons. To date, no studies have compared how sensitive the overall rCBF or BOLD predictions are to these alternatives.

The output of the neurovascular coupling module is a blood flow-inducing signal, l , that serves as the input signal for the vascular model. Many early synthetic brain imaging studies simply used the synaptic activity measure p . However it is known that synaptic activity does not directly drive changes in blood flow, but several mechanisms coexist to regulate blood flow in response to neural activity including the neuron–astrocyte pathway (Koehler, Gebremedhin, & Harder, 2006), vasomotor GABAergic interneurons (Cauli et al., 2004), and nitric oxide (NO) diffusion (Metea & Newman, 2006). It is therefore becoming increasingly popular to use a generic blood flow-inducing signal that subsumes these different mechanisms as input to a vascular model, as suggested by Friston, Mechelli, Turner, and Price (2000). We use a modified version of Riera et al.'s (2006) formulation of this signal that normalizes the synaptic activity signal to account for differences in the number of neurons in the model region compared to the actual brain region (see Section 2).

Poznanski and Riera (2006) review synthetic brain imaging approaches and argue for the need to model networks of astrocytes connected via gap-junctions and connected to the vascular system. While we agree in principle, the data needed to construct models of integrated neurons, glia and blood supply is not available. Instead, our primary concern is to base our predictions of imaging results on models of neural circuitry underlying some range of human behavior which make contact with related data from animal neurophysiology on the activity of single neurons. Moreover, it is possible to gain significant insight into the large scale organization of the brain by modeling the neural networks alone, and at a coarser grain, if the model is constrained by enough experimental data. Synthetic brain imaging (Arbib, Fagg, & Grafton, 2003) on the FARS model of primate control of grasping (Fagg & Arbib, 1998) predicted the influence of PFC on the anterior intraparietal area AIP ten years before it was verified anatomically (Borra et al., 2007) and functionally (Baumann, Fluet, & Scherberger, 2009).

1.3. Vascular signal generation

The first synthetic brain imaging approaches (Arbib et al., 1995; Tagamets & Horwitz, 1998) were applied to PET data since it measures rCBF and therefore does not include some of the nonlinearities of the BOLD signal which also involves changes in blood

volume and oxygenation. Synthetic fMRI studies began to involve measures of synaptic activity with functions representing the hemodynamic response in order to simulate the signal smoothing and delay seen in the BOLD signal. At the same time, models of the BOLD response to increased blood flow were developed which became collectively known as the “hemodynamics approach” and were used in later synthetic brain imaging techniques to apply computational models to fMRI data (Babajani, Nekooei, & Soltanian-Zadeh, 2005; Babajani & Soltanian-Zadeh, 2006; Babajani-Feremi, Soltanian-Zadeh, & Moran, 2008; Riera et al., 2006, 2004; Sotero et al., 2009).

The earliest applications of synthetic brain imaging to fMRI used basically the same technique as that used for PET, but modified the integration time in order to account for the slice acquisition time of fMRI scanners (Arbib, Billard, Iacoboni, & Oztup, 2000; Tagamets & Horwitz, 1999). Horwitz and Tagamets (1999) additionally convolved the total synaptic activity with a Poisson function in order to simulate hemodynamic delay. Deco et al. (2004) used an analytic hemodynamic response function (HRF) from Glover (1999) which was more accurate than any of the HRFs used in synthetic fMRI until then.

The hemodynamics approach utilizes biomechanical models of vasculature that incorporate changes in blood oxygenation and volume. These models originated in Buxton et al.’s (1998) “balloon model”, which has blood flow as its sole input and outputs a BOLD signal consisting of extra- and intra-vascular components. The main feature of this model is that it is able to reproduce the transients of the BOLD response such as the initial dip and post-undershoot. Friston et al.’s (2000) extension of the balloon model embeds it in a regional cerebral blood flow (rCBF) model of how a flow-inducing signal (described in Section 1.2) causes changes in blood flow. This was a linear dynamical model, assuming that the relationship between the signal and rCBF is linear and that nonlinearity comes in during the transformation from rCBF to the BOLD response.

2. Materials and methods

In order to facilitate both region- and voxel-based analysis of simulated PET and fMRI responses, modeled neurons in each region are grouped into virtual voxels (Fig. 1). Each virtual voxel contains an instantiation of the extended balloon model with Gaussian crosstalk between adjacent voxels (as in Babajani et al. (2005)). In the simulations described below we do not spatially locate voxels within regions and therefore do not exploit this crosstalk feature; however this is possible with more detailed neural models (see Section 4).

Synapses are modeled as exponential (AMPA, GABA_A) or bi-exponential conductances (NMDA, GABA_B). Exponentially decaying conductances are governed by the following equation:

$$g(t) = Ge^{-t/\tau} \quad (2)$$

where G is the maximal conductance (or weight) of that specific synapse, and τ is a synapse type-specific decay time constant. Similarly, bi-exponential synaptic conductances are given by:

$$g(t) = G \frac{\tau_2}{\tau_2 - \tau_1} (e^{-t/\tau_1} - e^{-t/\tau_2}) \quad (3)$$

where τ_1 and τ_2 are synapse type-specific decay and rise time constants (see the Appendix for parameter values for each synapse type). Synaptic currents are generated using these conductances and the associated reversal potential, E :

$$I(t) = g(t) (E - V_m) \quad (4)$$

where V_m is the membrane voltage.

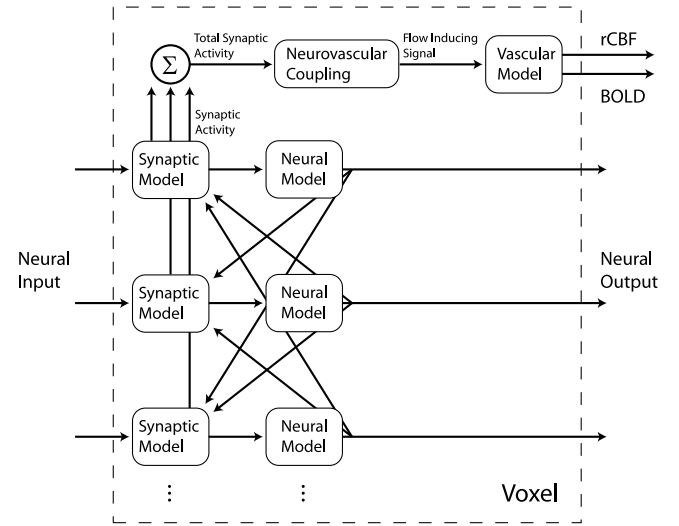


Fig. 1. Schematic for synthetic brain imaging models of the type presented here. The synapse model receives spiking input and provides synaptic conductance signals to the neural model. The synaptic conductances are summed and input to the neurovascular coupling component which provides input to the vascular model.

We sum the synaptic currents of each type (AMPA, NMDA, GABA_A, and GABA_B) and input the total synaptic current into the adaptive exponential LIF neural model (Brette & Gerstner, 2005):

$$I_{\text{total}}(t) = I_{\text{AMPA}}(t) + I_{\text{NMDA}}(t) + I_{\text{GABA}_A}(t) + I_{\text{GABA}_B}(t) \quad (5)$$

$$C \frac{dV_m}{dt} = g_L (E_L - V_m) + g_L \Delta_T e^{\frac{V_m - V_T}{\Delta_T}} + I_{\text{total}} \quad (6)$$

where C is the membrane capacitance, g_L is the leak conductance, E_L is the resting potential, Δ_T is the slope factor (which determines the sharpness of the voltage threshold), and V_T is the threshold voltage. Networks are constructed by grouping neurons into populations of pyramidal neurons and populations of inhibitory interneurons. Connections between neurons within and between populations are initialized probabilistically. Axonal conductance delays are implemented with delays randomized between 1 and 5 ms.

In order to simulate the hemodynamic response, we extend Riera et al.’s (2006) use of Friston et al.’s (2000) approach in grouping the various neurovascular coupling signals into a generic flow-inducing signal. We use Izhikevich and Edelman’s (2008) formulation of synaptic activity as the sum of synaptic conductances in all neurons in a voxel:

$$p(t) = \sum_m (g_{\text{AMPA}}^m(t) + g_{\text{NMDA}}^m(t) + g_{\text{GABA}_A}^m(t) + g_{\text{GABA}_B}^m(t)) \quad (7)$$

where the sum is over all neurons, m , in the virtual volume. Riera et al. (2006) introduced a baseline neurovascular coupling signal, p_0 , in generating the blood flow-inducing signal. However one problem with using this formulation in large-scale models with multiple regions is that of normalization according to the number of activated neurons. The number of neurons activated in a region affects the baseline neurovascular coupling signal, which would invalidate comparisons between regions and with experimental data. Furthermore, the blood flow-inducing signal is used as input to the balloon model, whose variables are in normalized units. Therefore, we extend Riera et al.’s formulation to normalize the neurovascular coupling signal according to its baseline level:

$$\frac{dl}{dt} = \varepsilon \left[\frac{p(t - \tau_h) - p_0}{p_0} \right] - \frac{l}{\tau_l} + \frac{(1 - f_{\text{in}})}{\tau_f} \quad (8)$$

where ε is the efficacy of the neurovascular coupling, p_0 is the baseline synaptic activity, f_{in} is the induced blood flow providing

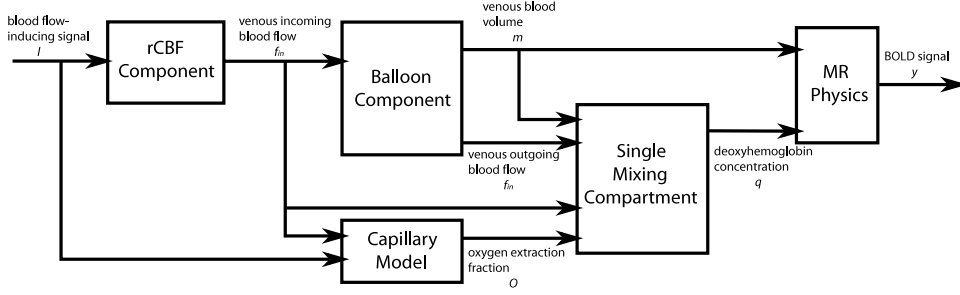


Fig. 2. The hemodynamic model used for these simulations. The rCBF component generates a change in incoming venous blood flow in response to a blood flow-inducing signal (the output of the neurovascular coupling component in Fig. 1). The balloon component describes the change in venous blood volume and outgoing blood flow in response to incoming venous blood flow. Zheng et al.'s capillary model describes the tissue extraction of oxygen from the capillary, and the single mixing compartment determines the concentration of deoxyhemoglobin. A model of MR physics generates a simulated BOLD signal from the venous blood volume and deoxyhemoglobin concentration.

feedback, and τ_i and τ_f are the time constants of the signal decay and autoregulatory feedback, respectively. The time constant values are based on the frequency of vasomotor constrictions and diffusion rate of nitric oxide (NO). The equation includes a delay time constant, τ_h , allowing the model to reflect the typical delay between the stimulus and the onset of the BOLD response. We set this parameter to 0 in order to improve simulation efficiency and since we are interested in the amplitude rather than the timing of the BOLD response. Multi-region models which build on this work would require that this parameter be fitted region-by-region to experimental data. However this fitting must be done with a neural model that includes realistic conductance delays in order to account for the portion of the delay that does not reflect the timing of neural processing.

We use Zheng et al.'s extension of the balloon model without modification to generate rCBF and BOLD signals from this blood-flow inducing signal (see Fig. 2). This system allows synthetic PET and fMRI signals to be generated simultaneously from each voxel by sampling the rCBF or BOLD signals, respectively, according to the repetition time (TR) of the scan. The change in the incoming venous blood flow, f_{in} , is given directly by

$$\frac{df_{in}}{dt} = l(t). \quad (9)$$

The balloon component of the model describes the change in venous blood volume, m , as the difference between the incoming and outgoing venous blood flow (f_{in} and f_{out} , respectively):

$$\tau_0 \frac{dm}{dt} = f_{in}(t) - f_{out}(t) \quad (10)$$

where τ_0 is the time constant of the venous compartment. The outgoing venous blood flow is a function of the venous volume:

$$f_{out}(t) = m(t)^{1/\alpha} \quad (11)$$

where the parameter α is known as Grubb's parameter. The change in the concentration of deoxyhemoglobin, q , depends on the incoming and outgoing venous blood flow, the fraction of oxygen extracted by the tissue, O , and the venous blood volume:

$$\tau_0 \frac{dq}{dt} = f_{in}(t) \frac{O(t)}{O_0} - f_{out}(t) \frac{q(t)}{m(t)} \quad (12)$$

where O_0 is the baseline oxygen extraction fraction.

The portion of the balloon model which involves the way in which blood flow affects oxygen delivery to tissue (originally developed by Buxton & Frank, 1997) was updated by Zheng et al. (2002). The balloon model only applied to steady-state conditions. Zheng et al.'s model includes a compartment for tissue oxygen and a full capillary model with dynamics in order to be applicable

to transient as well as steady-state conditions. In this model the fraction of capillary oxygen extracted by the tissue, O , is given by

$$\frac{\varphi}{f_{in}(t)} \frac{dO}{dt} = -O(t) + (1 - h(t)) \left[1 - \left(1 - \frac{O_0}{1 - h_0} \right)^{1/f_{in}(t)} \right] \quad (13)$$

where φ is a constant related to mean capillary transit time and h_0 is the baseline ratio of tissue and arterial plasma oxygen concentrations. The variable h is the ratio of tissue oxygen concentration and plasma oxygen concentration at the arterial end of the capillary:

$$J \frac{V_{tis} C_p T_c}{V_{cap} C_B O_0} \frac{dh}{dt} = \left(\frac{\bar{C}_B(t) - h(t) C_B^a}{\bar{C}_{B_0} - h_0 C_B^a} - 1 \right) - K_m l(t) \quad (14)$$

where J is a scaling constant for tissue transport time, V_{tis}/V_{cap} is the ratio of volume of blood in the tissue to volume of blood in the capillary, C_p/C_B is the ratio of oxygen concentration in plasma to total oxygen concentration in blood, T_c is the capillary transit time, C_B^a is the blood oxygen concentration in the arterial end of the capillary, and the parameter K_m controls the change in metabolic demand with neural activity. The mean capillary oxygen concentration, \bar{C}_B , is given by:

$$\frac{\varphi}{f_{in}(t)} \frac{d\bar{C}_B}{dt} = -\bar{C}_B(t) - \frac{C_B^a O(t)}{\ln \left(1 - \frac{O(t)}{1 - h(t)} \right)} + C_B^a h(t). \quad (15)$$

The resulting BOLD signal, y , is a function of the deoxyhemoglobin concentration and venous blood volume:

$$y(t) = V_0 [(k_1 + k_2) (1 - q(t)) - (k_2 + k_3) (1 - m(t))] \quad (16)$$

where V_0 is the resting blood volume fraction and k_1 , k_2 , and k_3 are parameters that can be set to simulate different magnetic field strengths (B_0) and echo times (TE). We tested values computed for two scan configurations: $B_0 = 4.7$ T, TE = 20 ms and $B_0 = 1.5$ T, TE = 40 ms. Both sets of resulting parameter values yielded similar results for the simulations we performed. Here we report results using k_1 , k_2 , and k_3 values corresponding to $B_0 = 1.5$ T and TE = 40 ms (see the Appendix for parameter values).

Our WTA network model contained one population of 400 inhibitory interneurons and two populations each with 800 excitatory pyramidal cells (2000 neurons total, Fig. 3). Task-related input to pyramidal cells in each excitatory population came from associated pools of 500 Poisson spike generators firing at a frequency proportional to the confidence level for the response option represented by that population. Each Poisson spike generator was connected to an AMPA or NMDA synapse on each neuron in its corresponding pyramidal population with probability 0.1. In order to simulate non-task-related input, each neuron received excitatory projections (AMPA or NMDA synapses) from a common pool of 500 Poisson spike generators firing at 20 Hz

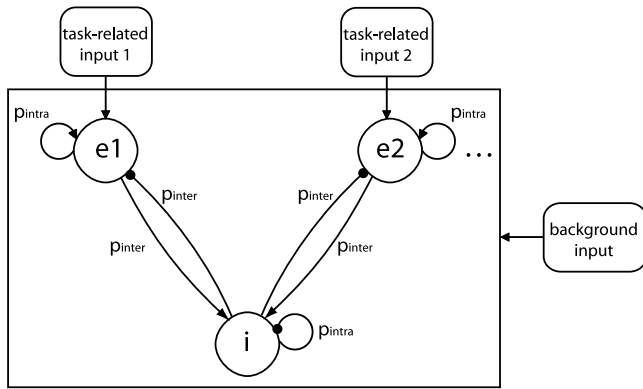


Fig. 3. The WTA network used in these simulations. Arrows denote excitatory projections and filled circles represent inhibitory projections. For each response option, a population of excitatory pyramidal neurons (e1 and e2 in these simulations) is reciprocally connected with a single population of inhibitory interneurons (i). Each neuron in each excitatory population is also probabilistically connected to other neurons in the same population. The connections are labeled with parameters p_{intra} and p_{inter} which define the probability that a neuron in one population will project to a neuron in another population (or the same population in the case of reciprocal connections). All neurons receive background input and excitatory populations additionally receive task-related inputs.

with a connection probability of 0.1. Recurrent connections within populations were governed by a single parameter p_{intra} , which is the probability that each pyramidal cell projected to an AMPA or NMDA synapse on other pyramidal cells in the same population, and that each inhibitory interneuron projected to a GABA_A or GABA_B synapse on other interneurons in the same population. Pyramidal cells of each population projected to AMPA or NMDA synapses on the inhibitory interneurons with probability p_{inter} , and each inhibitory interneuron projected to GABA_A or GABA_B synapses on the pyramidal cells with the same probability p_{inter} . Note that parameters for which a range of values are given by the neurophysiological literature, such as maximal synaptic conductance, were randomized in that range (Naud, Marcille, Clopath, & Gerstner, 2008). The only parameters left free to vary were the two connection probabilities p_{intra} and p_{inter} . The large-scale connectivity between populations was therefore fixed, but the connectivity between individual neurons in those populations was randomly generated according to the connection probability parameters.

The model was implemented in the Python programming language using the Brian simulator Goodman and Brette (2008). Simulations were run on a network of Linux computers using custom cluster management software.

3. Results

In order to test the model, we ran it with a series of inputs with varying levels of contrast between their firing rates. We defined

contrast as the ratio between the absolute difference of the task-related inputs and the total input stimulation, $\frac{|t_1 - t_2|}{t_1 + t_2}$, where t_1 and t_2 are the firing rates of the task-related input pools. This value is meant to correspond to variables in decision-making tasks such as coherence in the RDMDD task (Newsome, Britten, & Movshon, 1989). For example, at a contrast level of 0 both task-related Poisson spike generator pools fired at 20 Hz (representing no preference for either response options), at 0.25 one fired at 25 Hz and the other at 15 Hz, and at 1.0 one fired at 40 Hz and the other at 0 Hz (representing total confidence in one response option). Crucially, the total amount of stimulation to the network was always the same (40 Hz), meaning that any difference in the rCBF response during the conditions is due to the structure of the input and intra-regional network activity in response to it, rather than differences in the total amount of stimulation received by the network. The network was run for 20 s with a time step of 0.1 ms and stimulus duration of 0.5 s. Each contrast level (0, 0.0625, 0.125, 0.25, 0.5, and 1.0) was tested in 10 trials.

3.1. Example network activity

The network spiking activity given inputs with a contrast of 0.25 (25 Hz task-related stimulation to e1 and 15 Hz to e2) in a representative network ($p_{\text{intra}} = 0.07$, $p_{\text{inter}} = 0.05$) and trial is shown in Fig. 4. When the task-related stimulation was applied, the neurons in both excitatory populations quickly began to fire at high frequencies and activate interneurons in the inhibitory population. The interneurons quickly inhibited the pyramidal cells in each excitatory population, but since e1 had already reached a higher initial peak firing rate (65 Hz compared to 30 Hz in e2), it was able to rebound more quickly from the inhibition and maintain a steady state of activity while inhibiting e2 via the inhibitory interneurons. The inhibitory population reached a mean peak firing rate of about 5 Hz during the stimulation period. At the end of the stimulation period, the excitatory population receiving the highest frequency input stimulation (e1) reached a mean peak firing rate of about 35 Hz, while the other excitatory population (e2) was inhibited and fired at around 5 Hz (Fig. 5).

To measure the network's performance in a decision-making task, we treated the network as a classifier, using the mean firing rate of an excitatory population during the last 100 ms of the stimulus (normalized by the total mean firing rate over both excitatory populations) as the predicted probability that it is receiving the maximal input. If the difference between the firing rates of the excitatory populations was above some threshold, γ , the response option corresponding to the maximally firing excitatory population was declared as chosen. We then generated receiver operating characteristic (ROC) curves for each response option by varying this threshold and computing the false positive and true positive rates for 20 sample input patterns. We computed

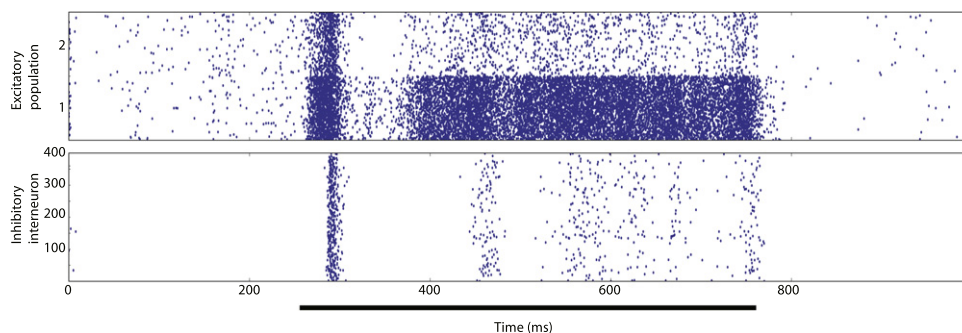


Fig. 4. Spiking activity of the two excitatory neuron populations (top) and inhibitory interneurons (bottom) in response to inputs at 25 Hz (task-related input 1) and 15 Hz (task-related input 2). The duration of the task-related input stimulation is shown by the horizontal bar.

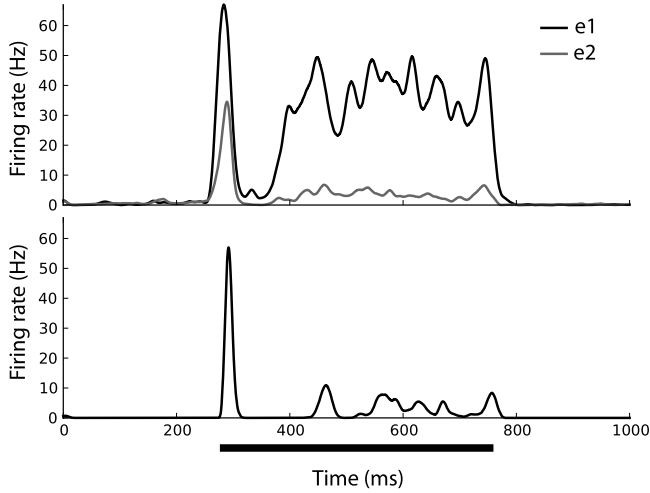


Fig. 5. Firing rate of the two excitatory populations (top) and inhibitory interneurons (bottom) for the same network and during the same trial as that shown in Fig. 4 (task-related input 1 = 25 Hz, task-related input 2 = 15 Hz). The duration of the task-related input stimulation is shown by the horizontal bar.

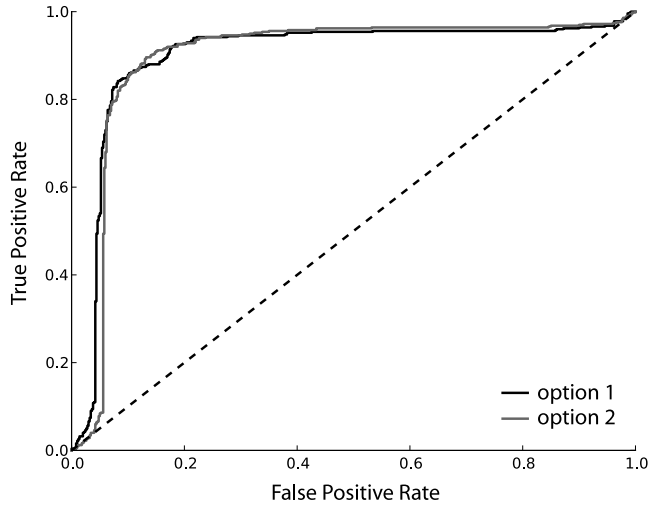


Fig. 6. ROC curves for each response option for the example network whose activity is shown in Figs. 4 and 5 (total AUC = 0.90). The dotted line shows the performance at chance.

the total area under the curve (AUC, Fawcett, 2004) by summing the area under the ROC curve for each response option, weighted by that option's relative frequency in the sample input patterns. The ROC curves for the example network whose activity is shown in Figs. 3 and 4 ($p_{\text{intra}} = 0.03$, $p_{\text{inter}} = 0.04$) is shown in Fig. 6. This network's performance is much better than chance with a total AUC of 0.90 (compared to chance at 0.5).

The total synaptic activity, $p(t)$, and generated BOLD signal for the example network and trial shown in Figs. 3 and 4 is shown in Fig. 7. The total synaptic activity is shown for 1 s of the trial including the 250 ms before and after the stimulus. This includes excitatory (AMPA, NMDA) and inhibitory (GABA_A , GABA_B) conductances in both pyramidal cells and inhibitory interneurons. The properties of the balloon model result in an integrated and delayed response with a peak within the range of reported BOLD responses and the characteristic post-stimulus undershoot. In order to characterize the relationship between the peak of the BOLD response and the computations performed by the network, we fit a linear function to the data. Fig. 8 shows the data points and fitted function for the example network shown in Figs. 3–6. This particular network exhibited a positive relationship between

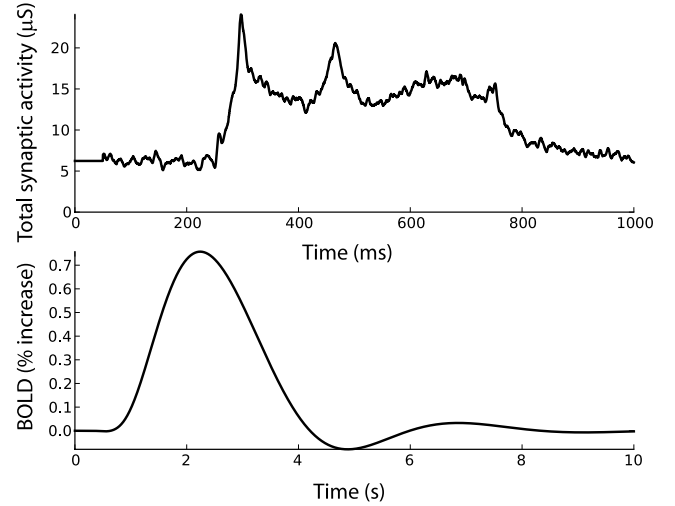


Fig. 7. Total synaptic activity (top) and generated BOLD signal (bottom) for the example network and trial from Figs. 4 and 5.

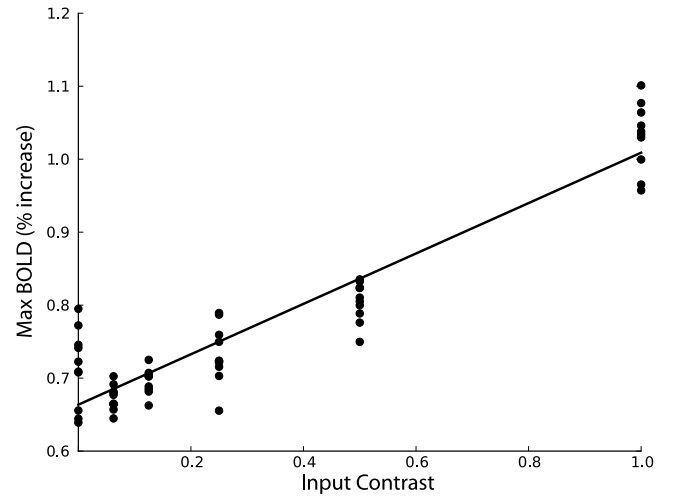


Fig. 8. The peak of the BOLD response in each trial with different input contrast levels (dots) and the fitted linear function (solid line, slope = 0.3, $R^2 = 0.878$).

the input contrast and BOLD response (slope = 0.3, $R^2 = 0.878$), yielding a stronger BOLD response as the task difficulty decreased (input contrast increased).

3.2. Parameter space analysis

In order to determine the general properties of our WTA network, we performed a grid search over the values for the parameters p_{intra} and p_{inter} in the range 0.01 to 0.1. The total AUC for the network with each tested parameter value combination is shown in Fig. 9(a). The network reaches peak performance when the recurrent connection probability, p_{intra} , is at least 0.04 and slightly greater than the inter-population connection probability, p_{inter} . Fig. 9(b) shows the slope of the line fitted to the input contrast–max BOLD data for each parameter combination tested. The regions of parameter space that result in the best performance (highest AUC) also appear to result in a positive relationship between input contrast and the peak of the BOLD response (as in the example shown in Fig. 8). Most parameter value combinations yield a slope close to zero, while a small region results in poor task performance and a negative relationship between input contrast and peak BOLD response.

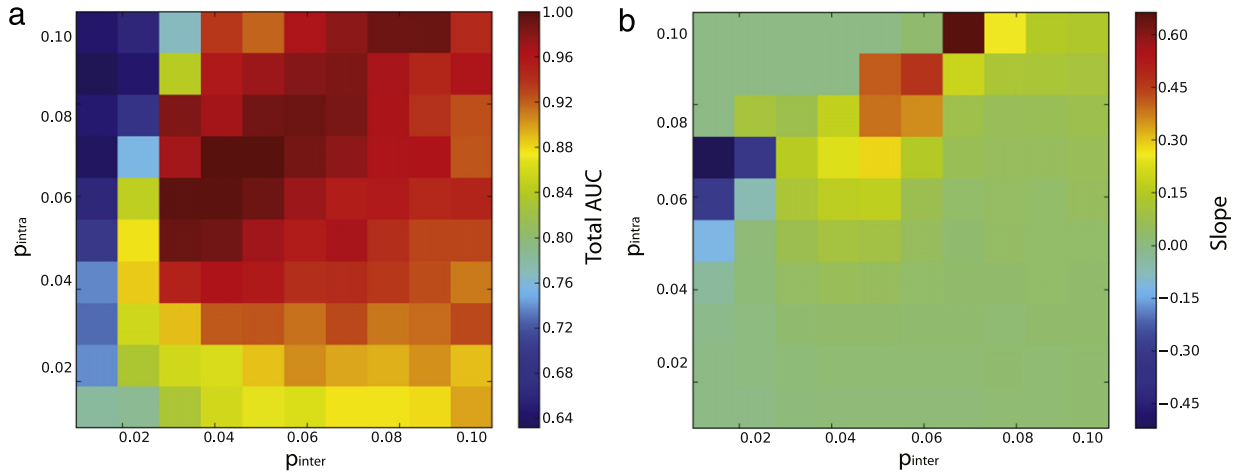


Fig. 9. (A) The total AUC of the WTA network for all tested values of the parameters p_{intra} and p_{inter} . (B) The slope of the linear function fitted to the input contrast–max BOLD relationship for all tested values of the parameters p_{intra} and p_{inter} .

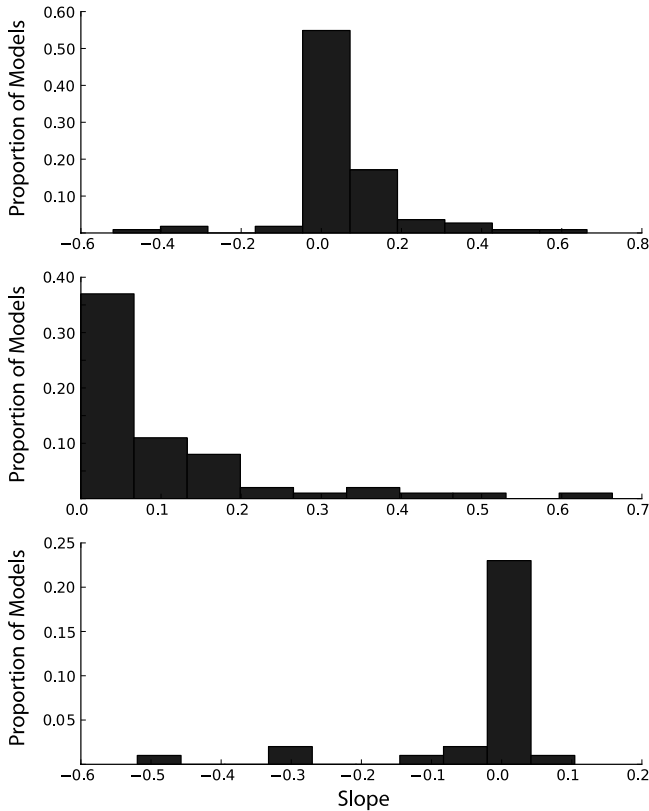


Fig. 10. Distribution of the slope of the fitted input contrast–max BOLD linear function. Top: Distribution over all tested parameter value combinations. Middle: Distribution over all parameter value combinations which yield a total AUC of 0.90 or greater. Bottom: Distribution over parameter values which result in a total AUC of less than 0.90.

In order to determine the relationship between the performance of the network and its BOLD signature, we analyzed the distribution of input contrast–max BOLD slopes in network instances with a total AUC above and below a given threshold. Fig. 10 shows these distributions for all parameter values (top), those with a total AUC above the threshold (middle) and those with an AUC below the threshold (bottom). The AUC threshold used here was 0.90. In the full range of tested parameter values the network is equally likely to exhibit a negative or positive relationship between the input contrast and the peak of the BOLD response. However, networks that can accurately perform the task (have a total AUC above the

threshold) only yield positive input contrast–max BOLD relationships, while those that cannot perform the task accurately are more likely to result in a negative relationship. We then examined how the distribution of input contrast–max BOLD slope for networks with an AUC above a given threshold changes as the threshold is varied from 0.5 to 0.99 (Fig. 11). As the threshold is increased, the distribution skews more and more to positive slope values, until with thresholds above 0.95 the slope values are exclusively positive.

4. Discussion

We have shown that a WTA network commonly used in neural models of decision-making predicts a clear relationship between the structure of its inputs and the peak of the resulting BOLD response. Without the constraint of having to actually perform the decision-making task, the model predicts a range of BOLD responses depending on the parameters. However, if the model is required to have accurate performance on the task, it predicts a positive relationship between the input contrast and peak of the BOLD signal. If the model were being compared to an anatomical region-of-interest (ROI) analysis, it would have to yield the observed activation in the experiment. However, an analysis which seeks to investigate the neural substrate of a cognitive process searches for voxels throughout the entire brain which have a BOLD response matching some prediction from the cognitive model. Synthetic brain imaging allows precise predictions for fMRI experiments to be generated from computational models that can also make contact with neurophysiological and behavioral data. The resulting models therefore provide a mechanistic description of neural dynamics that is doubly causal—explaining their effects on both behavior and hemodynamic signals.

Similar to the behavior of the neurons in our WTA model, single-unit recordings in monkeys show increases in activity in regions involved in decision-making such as the dorsolateral prefrontal cortex (DLPFC, Kim & Shadlen, 1999) and the lateral intraparietal area LIP (Shadlen & Newsome, 2001). These increases occur at a slower rate with increasing trial difficulty, suggesting that these regions play a role in integrating information. Our WTA model implements this computation via the recurrent projections in the excitatory populations, but additionally compares the evidence between response options via the inhibitory projections. Recurrent neural circuit models such as this one more accurately match LIP activity and response times during perceptual decision-making tasks than diffusion models (Wang, 2008). Our model's two free parameters, p_{inter} and p_{intra} , control the strength of projections

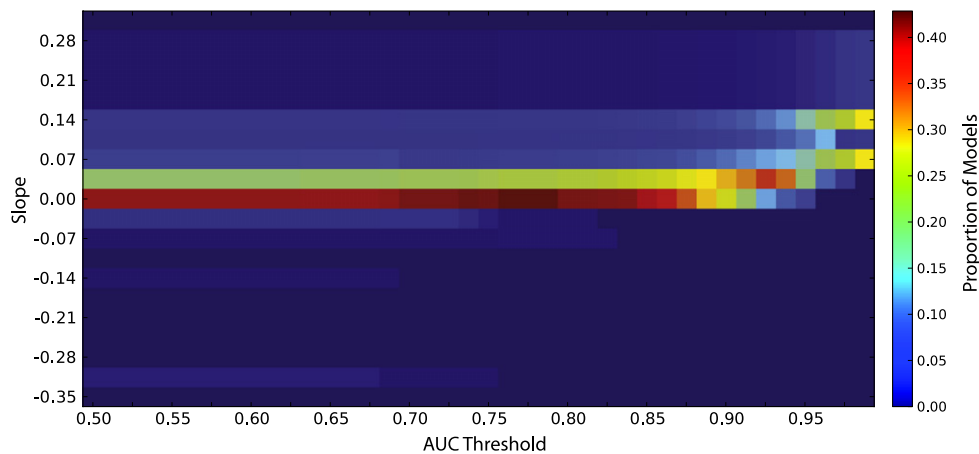


Fig. 11. Distribution of the slope of the input contrast-max BOLD linear function (y axis) for parameter value combinations with an AUC above a given threshold, as the threshold is varied from 0.5 to 1.0 (x axis).

within and between neural populations, respectively. Our simulations predict that accurate performance in decision-making tasks relies on strong recurrent projections within homogeneous neural populations.

Our simulation results predict an increase in BOLD response with decreasing task difficulty (higher contrast) for voxels containing WTA networks like the one we used. Human imaging studies have found several regions which exhibit this pattern of BOLD activation during decision-making tasks including the DLPFC and inferior parietal lobule (Heekeren, Marrett, Ruff, Bandettini, & Ungerleider, 2006; Kovacs, Cziraki, & Greenlee, 2010). Our results suggest that these regions functionally correspond to the DLPFC and LIP in the monkey and contain neural circuits similar to the WTA network presented here.

Synthetic brain imaging bears some similarities to Dynamic Causal Modeling (DCM) but there are important differences. Both techniques build generative (forward) models of the BOLD response, couple this response with a model of neural dynamics, and fit their parameters to fMRI data. However, DCM for fMRI typically uses a simple deterministic model of neural dynamics in a graph of nodes where, crucially, each node represents a brain region (Friston, Harrison, & Penny, 2003). The equations for each node define how activity in the corresponding region changes with the task and the activities of other nodes. Bayesian techniques are used to compute the posterior distribution of the coupling strengths between nodes and the modulation of those couplings by the task, given the observed fMRI data. In contrast, synthetic brain imaging focuses on neurons as the units of analysis, with each brain region modeled as a neurophysiologically plausible neural network. It thus yields insights into the emergent properties of large-scale networks that yield the BOLD response. Detailed models of each brain region thought to be involved in the task are created with the network connections defined using neurophysiological data from homologous regions of, e.g., the macaque brain and/or human anatomical data from diffusion tensor imaging (DTI) or tract tracing studies. Most synthetic brain imaging models must also perform the same task performed by the fMRI subject, further constraining the model and allowing comparisons to be drawn against psychophysical and hemodynamic measures. DCM therefore captures the overall activation levels of activity in a network of brain regions due its functional connectivity, whereas synthetic brain imaging focuses on the effects of intra- and inter-regional computations on the BOLD response. More specifically, synthetic brain imaging models interactions within regions in addition to those between regions so that it succeeds to the extent that it accounts not only for brain imaging data but also for the behaviors with which those data are

correlated and, where detailed homologies exist, for neurophysiological recordings of single-cell activity in closely related species such as the macaque. The two techniques are not mutually exclusive. Indeed, coupling parameters computed in a DCM analysis can be used to constrain projection strengths in a synthetic brain imaging model, which can then be run with novel tasks and stimuli to make predictions for future fMRI experiments.

Directions for future work concerning the synthetic brain imaging technique are spatial localization of virtual voxels with consideration of inter-voxel interactions and inclusion of the effects of modulatory neurotransmitters on global cerebral blood flow (CBF). The technique we currently use groups neurons from each region into virtual voxels but does not spatially locate the voxel within the region. To date, only one study has localized simulated neurons in voxels obtained from human MRI data (Izhikevich & Edelman, 2008), but this study did not look at the effects of task-related neural activity on the simulated fMRI signal. Only two studies have simulated the crosstalk in the neurovascular coupling mechanism from adjacent voxels (Babajani et al., 2005; Babajani & Soltanian-Zadeh, 2006), but neither of these was conducted on a large-scale neural model. Our plan for future work involves using standard brain atlases (such as the MNI or Talairach atlases) and available neurophysiological and hodological data to assign each voxel a spatial location. The atlas will provide a list of coordinates for each brain region. Many neurophysiological and tract tracing studies describe the distribution of neurons with various functional and connectivity properties within a region in terms of gradients (i.e. neurons in region x project to region y in a dorsal-ventral gradient with the strongest connections in the dorsal-most region). This information will be used to probabilistically designate a neuron to a coordinate within a region based on its response properties and connection strengths. Multiple virtual subjects will be generated using this stochastic voxel localization method to simulate inter-subject anatomical and functional variability. This will allow simulation of crosstalk between adjacent voxels (as Babajani et al., 2005 do using spatial convolution with a Gaussian kernel, for example) and generation of statistical parametric maps of significantly activated voxels for direct comparison with those reported in experimental studies.

As pointed out by Attwell and Iadecola (2002) and Poznanski and Riera (2006), other neurotransmitters and neuromodulators such as dopamine, serotonin, and noradrenaline might globally modulate CBF. Krimer, Muly, Williams, and Goldman-Rakic (1998) have shown that the axons of dopaminergic neurons innervate cortical microvessels and that dopamine induces vasomotor responses *in vitro*. This complicates the interpretation of brain imaging studies in patients with conditions such as schizophrenia and

Table A.1

Parameter values for the neural model used in the simulations.

Parameter	Description	Value
G_{AMPA}	Maximum conductance of AMPA synapses	Uniformly random in range 0.35–1 nS
G_{NMDA}	Maximum conductance of NMDA synapses	Uniformly random in range 0.01–0.1 nS
$G_{\text{GABA}-A}$	Maximum conductance of GABA _A synapses	Uniformly random in range 0.25–1.2 nS
$G_{\text{GABA}-B}$	Maximum conductance of GABA _B synapses	Uniformly random in range 0.1–0.6 nS
τ_{AMPA}	Decay time constant of AMPA synaptic conductance	2.5 ms
$\tau_1\text{--NMDA}$	Decay time constant of NMDA synaptic conductance	10 ms
$\tau_2\text{--NMDA}$	Rise time constant of NMDA synaptic conductance	100 ms
$\tau_{\text{GABA}-A}$	Decay time constant of GABA _A synaptic conductance	2.5 ms
$\tau_1\text{--GABA}-B$	Decay time constant of GABA _B synaptic conductance	10 ms
$\tau_2\text{--GABA}-B$	Rise time constant of GABA _B synaptic conductance	100 ms
E_{AMPA}	Reversal potential of AMPA-induced currents	0 mV
E_{NMDA}	Reversal potential of NMDA-induced currents	0 mV
$E_{\text{GABA}-A}$	Reversal potential of GABA _A -induced currents	−70 mV
$E_{\text{GABA}-B}$	Reversal potential of GABA _B -induced currents	−95 mV
C	Membrane capacitance	104 pF (pyramidal cells), 59 pF (interneurons)
g_L	Leak conductance	4.3 nS (pyramidal cells), 2.9 nS (interneurons)
E_L	Resting potential	−65 mV (pyramidal cells), −62 mV (interneurons)
Δ_T	Slope factor	0.8 mV (pyramidal cells), 3 mV (interneurons)
V_T	Voltage threshold	−52 mV (pyramidal cells), −42 mV (interneurons)

Table A.2

Parameter values for the neurovascular coupling model used in the simulations.

Parameter	Description	Value
ε	Synaptic efficacy in inducing blood flow	0.5
p_0	Baseline synaptic activity	Mean total synaptic activity over 200 ms without simulation
τ_h	Blood flow delay time constant	0 s
τ_s	Neurovascular coupling signal decay time constant	0.8 s
τ_f	Neurovascular coupling autoregulatory time constant	0.4 s

Table A.3

Parameter values for the vascular model used in the simulations.

Parameter	Description	Value
a	Grubb's parameter	0.38
φ	Constant related to mean capillary transit time	0.15 T_c
τ_0	Time constant of the venous compartment model	0.3 s
O_0	Baseline oxygen extraction fraction	0.34
h_0	Baseline ratio of tissue and arterial plasma oxygen concentration	0.1
$V_{\text{tis}}/V_{\text{cap}}$	Ratio of volume of blood in the tissue to volume of blood in the capillary	50
C_p/C_B	Ratio of oxygen concentration in plasmas to total oxygen concentration in blood	0.01
T_c	Capillary transit time	0.2 s
C_B^a	Blood oxygen concentration in the arterial end of the capillary	1.0
K_m	Gain for the change in metabolic demand with neural activity	0.05
V_0	Baseline venous blood volume fraction	0.02
k_1	MR physics model parameter	3.69
k_2	MR physics model parameter	2.41
k_3	MR physics model parameter	0.44

Parkinson's. For example, serotonin and certain Parkinson's treatments result in dissociation between CBF and neural metabolism (Cohen, Bonvento, Lacombe, & Hamel, 1996; Hirano et al., 2008). If synthetic brain imaging can be extended to include the effects of the altered amines on global CBF, it could become a powerful tool for the interpretation of clinical neuroimaging studies in terms of computational models of brain function.

Appendix

See Tables A.1–A.3.

References

- Amari, S. (1977). Dynamics of pattern formation in lateral-inhibition type neural fields. *Biological Cybernetics*, 27(2), 77–87.
- Arbib, M. A., Billard, A., Iacoboni, M., & Oztop, E. (2000). Synthetic brain imaging: grasping, mirror neurons and imitation. *Neural Networks*, 13(8–9), 975–997.
- Arbib, M. A., Bischoff, A., Fagg, A. H., & Grafton, S. T. (1995). Synthetic PET: analyzing large-scale properties of neural networks. *Human Brain Mapping*, 2(4), 225–233.
- Arbib, M. A., Fagg, A. H., & Grafton, S. T. (2003). Synthetic PET imaging for grasping: from primate neurophysiology to human behavior. In F. T. Sommer, & A. Wichert (Eds.), *Exploratory analysis and data modeling in functional neuroimaging* (pp. 232–250). Cambridge MA: The MIT Press.
- Attwell, D., & Iadecola, C. (2002). The neural basis of functional brain imaging signals. *Trends in Neurosciences*, 25(12), 621–625.
- Aubert, A., Pellerin, L., Magistretti, P. J., & Costalat, R. (2007). A coherent neurobiological framework for functional neuroimaging provided by a model integrating compartmentalized energy metabolism. *Proceedings of the National Academy of Sciences of the United States of America*, 104(10), 4188–4193. <http://dx.doi.org/10.1073/pnas.0605864104>. doi: 0605864104 [pii].
- Babajani, A., Nekooei, M. H., & Soltanian-Zadeh, H. (2005). Integrated MEG and fMRI model: synthesis and analysis. *Brain Topography*, 18(2), 101–113.
- Babajani, A., & Soltanian-Zadeh, H. (2006). Integrated MEG/EEG and fMRI model based on neural masses. *IEEE Transactions on Biomedical Engineering*, 53(9), 1794–1801.
- Babajani-Feremi, A., Soltanian-Zadeh, H., & Moran, J. (2008). Integrated MEG/fMRI model validated using real auditory data. *Brain Topography*, 21(1), 61–74.
- Baumann, M. A., Fluet, M. C., & Scherberger, H. (2009). Context-specific grasp movement representation in the macaque anterior intraparietal area. *Journal of Neuroscience*, 29(20), 6436–6448. <http://dx.doi.org/10.1523/JNEUROSCI.5479-08.2009>. doi: 29/20/6436 [pii].
- Borra, E., Belmalih, A., Calzavara, R., Gerbella, M., Murata, A., Rozzi, S., et al. (2007). Cortical connections of the macaque anterior intraparietal (AIP) area. *Cerebral Cortex*.
- Brette, R., & Gerstner, W. (2005). Adaptive exponential integrate-and-fire model as an effective description of neuronal activity. *Journal of Neurophysiology*, 94, 3637–3642. United States.
- Buxton, R. B., & Frank, L. R. (1997). A model for the coupling between cerebral blood flow and oxygen metabolism during neural stimulation. *Journal of Cerebral Blood Flow & Metabolism*, 17(1), 64–72. <http://dx.doi.org/10.1097/00004647-199701000-00009>.
- Cauli, B., Tong, X., Rancillac, A., Serluca, N., Lambollez, B., Rossier, J., et al. (2004). Cortical GABA interneurons in neurovascular coupling: relays for subcortical vasoactive pathways. *Journal of Neuroscience*, 24(41), 8940.
- Cohen, Z., Bonvento, G., Lacombe, P., & Hamel, E. (1996). Serotonin in the regulation of brain microcirculation. *Progress in Neurobiology*, 50(4), 335.

- Corchs, S., & Deco, G. (2002). Large-scale neural model for visual attention: integration of experimental single-cell and fMRI data. *Cerebral Cortex*, 12(4), 339–348.
- Corchs, S., & Deco, G. (2004). Feature-based attention in human visual cortex: simulation of fMRI data. *NeuroImage*, 21(1), 36–45. doi: S1053811903005482 [pii].
- Deco, G., Rolls, E. T., & Horwitz, B. (2004). “What” and “where” in visual working memory: a computational neurodynamical perspective for integrating FMRI and single-neuron data. *Journal of Cognitive Neuroscience*, 16(4), 683–701.
- Fagg, A. H., & Arbib, M. A. (1998). Modeling parietal-premotor interactions in primate control of grasping. *Neural Networks*, 11(7–8), 1277–1303.
- Fawcett, T. (2004). *ROC graphs: notes and practical considerations for researchers*. Hewlett Packard Labs.
- Friston, K. J., Harrison, L., & Penny, W. (2003). Dynamic causal modelling. *NeuroImage*, 19(4), 1273–1302.
- Friston, K. J., Mechelli, A., Turner, R., & Price, C. J. (2000). Nonlinear responses in fMRI: the Balloon model, Volterra kernels, and other hemodynamics. *NeuroImage*, 12(4), 466–477.
- Glover, G. H. (1999). Deconvolution of impulse response in event-related BOLD fMRI. *NeuroImage*, 9(4), 416–429. doi: S1053811998904190 [pii].
- Goense, J. B., & Logothetis, N. K. (2008). Neurophysiology of the BOLD fMRI signal in awake monkeys. *Current Biology*, 18(9), 631–640.
- Goodman, D., & Brette, R. (2008). Brian: a simulator for spiking neural networks in python. *Frontiers in Neuroinformatics*, 2, 5.
- Heekeren, H. R., Marrett, S., Ruff, D. A., Bandettini, P. A., & Ungerleider, L. G. (2006). Involvement of human left dorsolateral prefrontal cortex in perceptual decision making is independent of response modality. *Proceedings of the National Academy of Sciences of the United States of America*, 103(26), 10023–10028. <http://dx.doi.org/10.1073/pnas.0603949103>.
- Hirano, S., Asanuma, K., Ma, Y., Tang, C., Feigin, A., Dhawan, V., et al. (2008). Dissociation of metabolic and neurovascular responses to levodopa in the treatment of Parkinson's disease. *Journal of Neuroscience*, 28(16), 4201. [http://dx.doi.org/10.1002/SICI1097-0193\(1999\)8:2/3<137::AID-HBM11>3.0.CO;2-B](http://dx.doi.org/10.1002/SICI1097-0193(1999)8:2/3<137::AID-HBM11>3.0.CO;2-B) [pii].
- Izhikevich, E. M., & Edelman, G. M. (2008). Large-scale model of Mammalian thalamocortical systems. *Proceedings of the National Academy of Sciences of the United States of America*, 105(9), 3593–3598. <http://dx.doi.org/10.1073/pnas.0712231105>. doi: 0712231105 [pii].
- Jueptner, M., & Weiller, C. (1995). Review: does measurement of regional cerebral blood flow reflect synaptic activity? Implications for PET and fMRI. *NeuroImage*, 2(2), 148–156.
- Kagan, I., Wilke, M., & Andersen, R.A. (2009). fMRI dynamics in monkeys reflect spatial decisions and preferences in free-choice and reward context tasks. Paper presented at the Soc. Neurosci.
- Kim, J. N., & Shadlen, M. N. (1999). Neural correlates of a decision in the dorsolateral prefrontal cortex of the macaque. *Nature Neuroscience*, 2(2), 176–185. <http://dx.doi.org/10.1038/5739>.
- Koehler, R. C., Gebremedhin, D., & Harder, D. R. (2006). Role of astrocytes in cerebrovascular regulation. *Journal of Applied Physiology*, 100(1), 307–317. <http://dx.doi.org/10.1152/jappphysiol.00938.2005>. doi: 100/1/307 [pii].
- Kovacs, G., Cziraki, C., & Greenlee, M. W. (2010). Neural correlates of stimulus-invariant decisions about motion in depth. *NeuroImage*, 51(1), 329–335. <http://dx.doi.org/10.1016/j.neuroimage.2010.02.011>.
- Krimer, L., Muly, E., Williams, G., & Goldman-Rakic, P. (1998). Dopaminergic regulation of cerebral cortical microcirculation. *Nature Neuroscience*, 1(4), 286–289.
- Metea, M. R., & Newman, E. A. (2006). Glial cells dilate and constrict blood vessels: a mechanism of neurovascular coupling. *Journal of Neuroscience*, 26(11), 2862–2870. <http://dx.doi.org/10.1523/JNEUROSCI.4048-05.2006>. doi: 26/11/2862 [pii].
- Naud, R., Marcille, N., Clopath, C., & Gerstner, W. (2008). Firing patterns in the adaptive exponential integrate-and-fire model. *Biological Cybernetics*, 99(4–5), 335–347.
- Nelissen, K., Luppino, G., Vanduffel, W., Rizzolatti, G., & Orban, G. A. (2005). Observing others: multiple action representation in the frontal lobe. *Science*, 310(5746), 332–336.
- Newsome, W., Britten, K., & Movshon, J. (1989). Neuronal correlates of a perceptual decision. *Journal of Neuroscience*, 9(12), 2580–2594.
- Palmer, J., Huk, A., & Shadlen, M. (2005). The effect of stimulus strength on the speed and accuracy of a perceptual decision. *Journal of Vision*, 5(5), 376–404.
- Pelled, G., Bergstrom, D. A., Tierney, P. L., Conroy, R. S., Chuang, K. H., Yu, D., et al. (2009). Ipsilateral cortical fMRI responses after peripheral nerve damage in rats reflect increased interneuron activity. *Proceedings of the National Academy of Sciences of the United States of America*, 106(33), 14114–14119. <http://dx.doi.org/10.1073/pnas.0903153106>.
- Poznanski, R. R., & Riera, J. J. (2006). fMRI models of dendritic and astrocytic networks. *Journal of Integrative Neuroscience*, 5(2), 273–326. doi: S0219635206001173 [pii].
- Riera, J. J., Wan, X., Jimenez, J. C., & Kawashima, R. (2006). Nonlinear local electrovascular coupling. I: a theoretical model. *Human Brain Mapping*, 27(11), 896–914.
- Riera, J. J., Watanabe, J., Kazuki, I., Naoki, M., Aubert, E., Ozaki, T., et al. (2004). A state-space model of the hemodynamic approach: nonlinear filtering of BOLD signals. *NeuroImage*, 21(2), 547–567.
- Shadlen, M., & Newsome, W. (2001). Neural basis of a perceptual decision in the parietal cortex (area LIP) of the rhesus monkey. *Journal of Neurophysiology*, 86(4), 1916.
- Sotero, R. C., Trujillo-Barreto, N. J., Jimenez, J. C., Carbonell, F., & Rodriguez-Rojas, R. (2009). Identification and comparison of stochastic metabolic/hemodynamic models (sMHM) for the generation of the BOLD signal. *Journal of Computational Neuroscience*, 26(2), 251–269. <http://dx.doi.org/10.1007/s10827-008-0109-3>.
- Tagamets, M. A., & Horwitz, B. (1998). Integrating electrophysiological and anatomical experimental data to create a large-scale model that simulates a delayed match-to-sample human brain imaging study. *Cerebral Cortex*, 8(4), 310–320.
- Tagamets, M. A., & Horwitz, B. (1999). Functional brain imaging and modeling of brain disorders. *Progress in Brain Research*, 121, 185–200.
- Usher, M., & McClelland, J. L. (2001). The time course of perceptual choice: the leaky, competing accumulator model. *Psychological Review*, 108(3), 550–592.
- Wang, X. J. (2008). Decision making in recurrent neuronal circuits. *Neuron*, 60(2), 215–234. <http://dx.doi.org/10.1016/j.neuron.2008.09.034>.
- Wilke, M., Kagan, I., & Andersen, R.A. (2009). BOLD responses during pharmacologically induced hemi-neglect in the parietal cortex. Paper presented at the Soc. Neurosci.
- Wilke, M., Kagan, I., & Andersen, R.A. (2010). Pulvinar inactivation alters cortical responses during spatial decision making. Paper presented at the Soc. Neurosci.
- Zheng, Y., Martindale, J., Johnston, D., Jones, M., Berwick, J., & Mayhew, J. (2002). A model of the hemodynamic response and oxygen delivery to brain. *NeuroImage*, 16(3 Pt 1), 617–637.